The Astronomical Journal, 166:44 (13pp), 2023 August https://doi.org/10.3847/1538-3881/acd8bf
© 2023. The Author(s). Published by the American Astronomical Society.
OPEN ACCESS

TOI-3785 b: A Low-density Neptune Orbiting an M2-dwarf Star

Luke C. Powers[1,2], Jessica Libby-Roberts[1,2], Andrea S. J. Lin[1,2], Caleb I. Cañas[1,2,3,20], Shubham Kanodia[1,2,4], Suvrath Mahadevan[1,2,5], Joe P. Ninan[6], Guðmundur Stefánsson[7,19], Arvind F. Gupta[1,2], Sinclaire Jones[7,8], Henry A. Kobulnicky[9], Andrew Monson[10], Brock A. Parker[9], Tera N. Swaby[9], Chad F. Bender[10], William D. Cochran[11], Leslie Hebb[12,13], Andrew J. Metcalf[14], Paul Robertson[15], Christian Schwab[16], John Wisniewski[17], and Jason T. Wright[1,2,18]

[1] Department of Astronomy & Astrophysics, 525 Davey Laboratory, The Pennsylvania State University, University Park, PA 16802, USA; lvp5301@psu.edu
[2] Center for Exoplanets and Habitable Worlds, 525 Davey Laboratory, The Pennsylvania State University, University Park, PA 16802, USA
[3] NASA Goddard Space Flight Center, 8800 Greenbelt Road, Greenbelt, MD 20771, USA
[4] Earth and Planets Laboratory, Carnegie Institution for Science, 5241 Broad Branch Road, NW, Washington, DC 20015, USA
[5] ETH Zurich, Institute for Particle Physics & Astrophysics, Switzerland
[6] Department of Astronomy and Astrophysics, Tata Institute of Fundamental Research, Homi Bhabha Road, Colaba, Mumbai 400005, India
[7] Department of Astrophysical Sciences, Princeton University, 4 Ivy Lane, Princeton, NJ 08540, USA
[8] Department of Astronomy, The Ohio State University, 4055 McPherson Laboratory, Columbus, OH 43210, USA
[9] Department of Physics & Astronomy, University of Wyoming, Laramie, WY 82070, USA
[10] Steward Observatory, The University of Arizona, 933 N. Cherry Avenue, Tucson, AZ 85721, USA
[11] McDonald Observatory and Center for Planetary Systems Habitability The University of Texas, Austin, TX, USA
[12] Physics Department, Hobart and William Smith Colleges, 300 Pulteney Street, Geneva, NY 14456, USA
[13] Department of Astronomy, Cornell University, 245 East Avenue, Ithaca, NY 14850, USA
[14] Air Force research laboratory, Kirtland AFB, Albuquerque, NM 87117, USA
[15] Department of Physics & Astronomy, University of California Irvine, Irvine, CA 92697, USA
[16] School of Mathematical and Physical Sciences, Macquarie University, Balaclava Road, North Ryde, NSW 2109, Australia
[17] George Mason University Department of Physics & Astronomy, 4400 University Drive, MS 3F3, Fairfax, VA 22030, USA
[18] Penn State Extraterrestrial Intelligence Center, 525 Davey Laboratory, The Pennsylvania State University, University Park, PA 16802, USA
Received 2023 April 5; revised 2023 May 17; accepted 2023 May 22; published 2023 July 4

Abstract

Using both ground-based transit photometry and high-precision radial velocity spectroscopy, we confirm the planetary nature of TOI-3785 b. This transiting Neptune orbits an M2-Dwarf star with a period of ∼4.67 days, a planetary radius of $5.14 \pm 0.16\ R_\oplus$, a mass of $14.95^{+4.10}_{-3.92}\ M_\oplus$, and a density of $\rho = 0.61^{+0.18}_{-0.17}$ g cm^{-3}. TOI-3785 b belongs to a rare population of Neptunes ($4\ R_\oplus < R_p < 7\ R_\oplus$) orbiting cooler, smaller M-dwarf host stars, of which only ∼10 have been confirmed. By increasing the number of confirmed planets, TOI-3785 b offers an opportunity to compare similar planets across varying planetary and stellar parameter spaces. Moreover, with a high-transmission spectroscopy metric of ∼150 combined with a relatively cool equilibrium temperature of $T_{\rm eq} = 582 \pm 16$ K and an inactive host star, TOI-3785 b is one of the more promising low-density M-dwarf Neptune targets for atmospheric follow up. Future investigation into atmospheric mass-loss rates of TOI-3785 b may yield new insights into the atmospheric evolution of these low-mass gas planets around M dwarfs.

Unified Astronomy Thesaurus concepts: Exoplanet astronomy (486); Radial velocity (1332); Transits (1711); M dwarf stars (982)

1. Introduction

The success of the Kepler (Borucki et al. 2010) and TESS missions (Ricker et al. 2015) have produced a catalog of over 5000 confirmed exoplanets. Multiple studies have leveraged these detections to derive planetary occurrence rates across a wide range of parameter spaces. Planetary occurrence rates around M-dwarf stars (the most common spectral type in our galaxy) are of particular interest. Using Kepler, Dressing & Charbonneau (2013) found that small, short-period planets (such as super-Earths and sub-Neptunes, $1.4\ R_\oplus < R_p < 4\ R_\oplus$) are more common around M dwarfs than that of the Neptune- and Jupiter-sized planets. According to the NASA Exoplanet Archive (Akeson et al. 2013) there are only ∼10 transiting planets within the Neptune radii bounds ($4\ R_\oplus < R_p < 7\ R_\oplus$) with confirmed masses orbiting M-dwarf stars, significantly less than the terrestrial population. The processes by which these larger Neptunes orbiting low-mass stars form is still an open question—one that requires a larger sample of planets to answer. Discovering and characterizing more of these planets with precise radius and mass measurements will continue to aid efforts to quantify occurrence and understand the specific mechanisms behind M-dwarf planetary formation.

We present a new planet inhabiting this sparsely populated M-dwarf Neptune parameter space, TOI-3785 b. We used a combination of ground-based photometric (transit) and spectroscopic (radial velocity) follow up to confirm this TESS discovered planet which we describe in Section 2. Using stellar spectra, we update the stellar parameters (Section 3) confirming that TOI-3785 is an inactive M dwarf. We derive precise mass and radius measurements for TOI-3785 b in Section 4. In Section 5 we highlight TOI-3785 b's place across a variety of stellar and planetary parameters and discuss its

[19] NASA Sagan Fellow.
[20] NASA Postdoctoral Program Fellow.

Original content from this work may be used under the terms of the Creative Commons Attribution 4.0 licence. Any further distribution of this work must maintain attribution to the author(s) and the title of the work, journal citation and DOI.

Table 1
Stellar Parameters

Parameter	Description	Value	Source
Main identifiers:			
TOI	TESS object of interest	3785	ExoFOP-TESS (NExScI 2022)
TIC	TESS input catalog	458419328	ExoFOP-TESS (NExScI 2022)
2MASS	...	J08433613 + 6304413	ExoFOP-TESS (NExScI 2022)
Gaia DR3	...	1044013542142711296	ExoFOP-TESS (NExScI 2022)
APASS	...	59229225	ExoFOP-TESS (NExScI 2022)
Equatorial coordinates:			
α_{J2000}	R.A.	8:43:36	ExoFOP-TESS (NExScI 2022)
δ_{J2000}	decl.	+65:03:41	ExoFOP-TESS (NExScI 2022)
Proper motion:			
μ_α	Proper motion (R.A.)	-42.86 ± 0.01	GAIA (DR3; Gaia Collaboration et al. 2022)
μ_δ	Proper motion (decl.)	-16.95 ± 0.01	GAIA (DR3; Gaia Collaboration et al. 2022)
Distance and maximum extinction:			
d	Geometric distance (pc)	79.4 ± 0.1	Bailer-Jones et al. (2021)
$A_{V,\max}$	Maximum visual extinction	0.03	Green et al. (2019)
Magnitudes:			
TESS	TESS mag	12.496 ± 0.007	ExoFOP-TESS (NExScI 2022)
g	PS1 g'mag	15.244 ± 0.013	PS1 Chambers et al. (2016), Magnier et al. (2020)
r	PS1 r'mag	14.076 ± 0.008	PS1 Chambers et al. (2016), Magnier et al. (2020)
y	PS1 y'mag	12.248 ± 0.022	PS1 Chambers et al. (2016), Magnier et al. (2020)
J	2M J mag	11.051 ± 0.026	2MASS (Cutri et al. 2003)
H	2M H mag	10.387 ± 0.029	2MASS (Cutri et al. 2003)
K	2M K mag	10.165 ± 0.022	2MASS (Cutri et al. 2003)
W1	WISE1 mag	10.034 ± 0.023	WISE (Wright et al. 2010)
W2	WISE2 mag	9.966 ± 0.019	WISE (Wright et al. 2010)
W3	WISE3 mag	9.860 ± 0.045	WISE (Wright et al. 2010)

potential for various in-depth studies into comparative planetology. We conclude and summarize this work in Section 6.

2. Observations

2.1. TESS Photometry

TOI-3785 (Table 1) was first observed in TESS Sector 20, from 2019 December 24 to 2020 January 20. Similar to the TOI-1899 (Cañas et al. 2020) and TOI-3629 (Cañas et al. 2022) systems, we identified TOI-3785 b as a planetary candidate using a custom pipeline to search for transiting candidates in short and long-cadence TESS data. This target was independently identified by the Quick Look Pipeline (Huang et al. 2020) when a 4.67 days transiting signal was flagged during an observation in long-cadence mode (1800 s exposure). An identical periodic signal from TOI-3785 was again observed by TESS in Sector 47 from 2021 December 30 to 2022 January 28 with a two-minute exposure time. We retrieved both long- and short-cadence sectors using the `lightkurve` package (Lightkurve Collaboration et al. 1812). The Pre-search Data Conditioning Simple Aperture Photometry (Jenkins et al. 2016) flux was used during our analysis (Caldwell et al. 2020). We show this photometry along with the best-fit model from our joint fit in Figure 1.

2.2. Ground-based Photometric Follow Up

2.2.1. Red Buttes Observatory 0.6 m

One transit of TOI-3785 b was observed on 2021 November 11 using the 0.6 m telescope at the Red Buttes Observatory (RBO) in Wyoming (Kasper et al. 2016). We observed TOI-3785 b using the Bessell I filter at an exposure time of 240 s, from an airmass of 1.26 to 1.08. The post-transit observations were cut short due to increased cloud cover (Figure 1).

2.2.2. ARC 3.5 m Telescope

We obtained one transit of TOI-3785 b on the night of 2022 April 5 using the Astrophysical Research Consortium (ARC) Telescope Imaging Camera (ARCTIC; Huehnerhoff et al. 2016) at the ARC 3.5 m Telescope at Apache Point Observatory (APO). This target was observed with ARCTIC's narrow-band Semrock filter (between 842 and 873 nm; Stefansson et al. 2017, 2018), with an exposure time of 56 s, in the quad amplifier, fast readout mode, and with 4×4 on-chip binning mode in effect. Relatively photometric skies and the use of this narrow-band Semrock filter (designed to avoid regions of telluric water absorption), enabled us to obtain high-precision photometry even at a significant airmass change (airmass 1.38–3.81) over the entirety of the transit event. The increasing airmass toward the end (airmass >3) resulted in significant scatter in the post-transit baseline (Figure 1).

2.2.3. NESSI at WIYN

The NN-EXPLORE Exoplanet Stellar Speckle Imager (NESSI; Scott 2018) is mounted on the WIYN 3.5 m telescope at Kitt Peak National Observatory (KPNO). We used NESSI speckle photometry to search for faint stellar targets in close proximity to TOI-3785 that may contaminate the primary, or introduce additional photometric error. We observed this target on 2022 April 17 in the Sloan z' filter (865–960 nm).

The 5σ contrast curve in Figure 2 reveals no bright ($\Delta z'$ mag < 4) stellar companions within a $0.3''$–$1.2''$ range of TOI-3785. We also include the 2D NESSI speckle image for TOI-3785 as an inset.

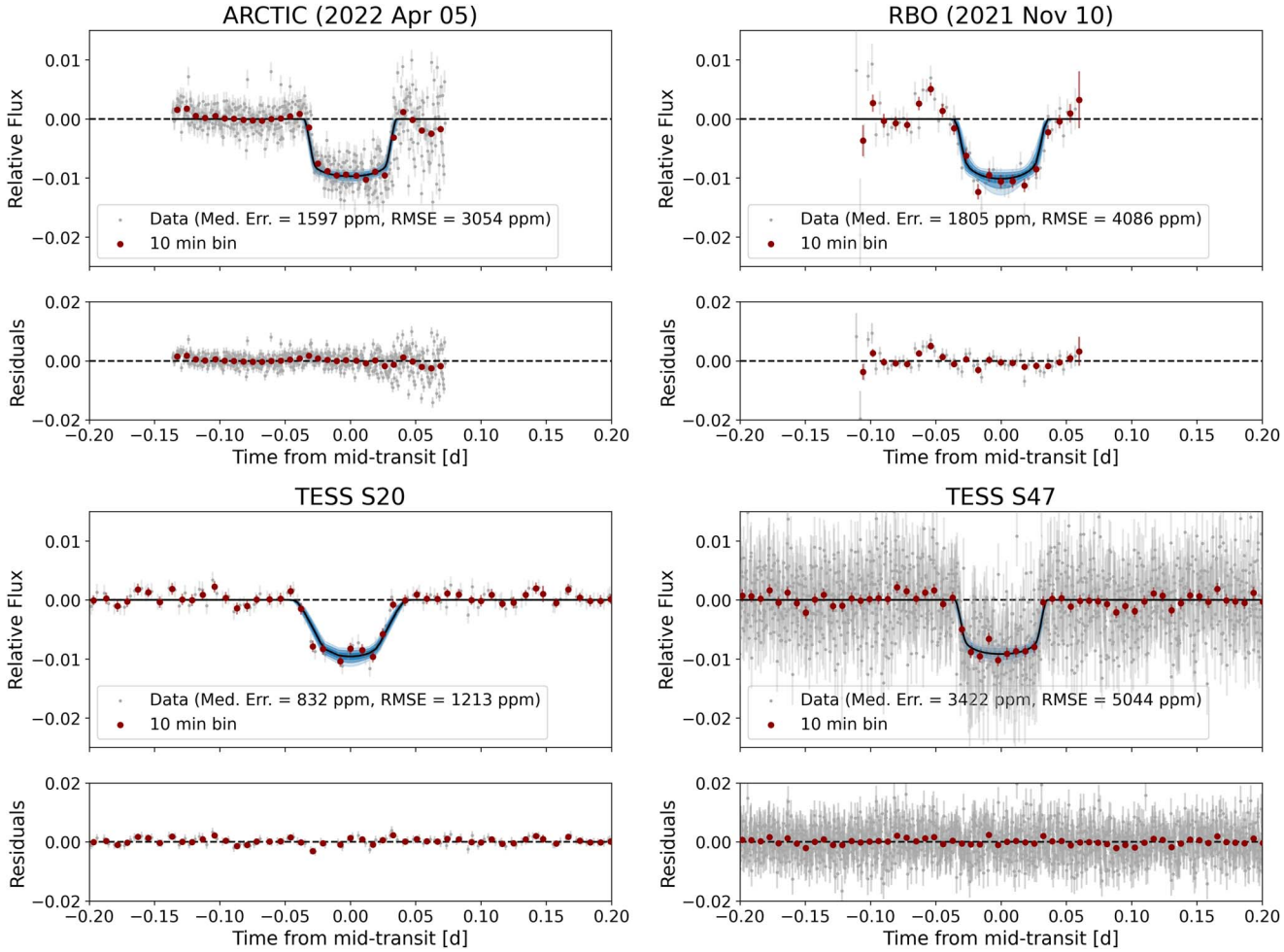

Figure 1. The transit observations conducted for TOI-3785 b. In each case, we fit a model to the light curve via `exoplanet` (Section 4). The best-fit model is shown in black, with the 1, 2, and 3σ confidence intervals in progressively lighter shades of blue. A 10 minute bin of our data is included as red points in each panel. It is also important to note that the reported median errors are dependent on their respective exposure time of the instrument used. The subpanels show the ARCTIC transit observed in the Semrock filter (top left), the RBO transit observed in Bessell I (top right), TESS Sector 20 data taken at long cadence (1800 s; bottom left), and TESS Sector 47 data taken at short cadence (120 s; bottom right).

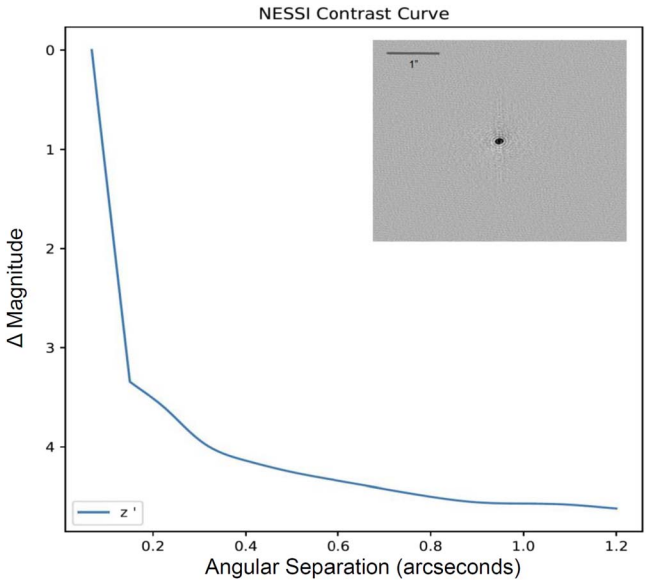

Figure 2. 5σ contrast curve from NESSI in Sloan z', showing no evidence of faint companions within 1.2″. Inset: The 2D reconstructed image of the 1.2″ region surrounding TOI-3785.

Additionally, we use Gaia Data Release 3 (DR3; Gaia Collaboration et al. 2022) to further rule out stellar companions within a 25″ range. According to Ziegler et al. (2018), Gaia has the capabilities to recover 93% of targets at a distance $> 2''$. In TOI-3785's case, Gaia DR3 reveals the closest object at 26″. Therefore, considering data from NESSI and Gaia, we can conclude that no source of significant photometric dilution is present from nearby stellar companions.

2.3. Radial Velocity Follow Up

2.3.1. The Habitable-zone Planet Finder

The Habitable-zone Planet Finder (HPF; Mahadevan et al. 2012, 2014) is designed to obtain high-precision near-infrared (808–1278 nm) radial velocity observations. Located on the 10 m Hobby–Eberly Telescope (HET; Ramsey et al. 1998; Hill et al. 2021) in Texas, this spectrograph is rigorously environmentally controlled (Stefansson et al. 2016) and fiber fed, allowing for simultaneous science and sky observations (Kanodia et al. 2018). From the raw HPF data, we correct for bias noise, cosmic rays, and nonlinearity using `HxRGproc` (Ninan et al. 2018).

Table 2
HPF RV Points of the High S/N Points used in the Analysis

BJD_{TDB}	RV ($m\,s^{-1}$)	σ ($m\,s^{-1}$)	S/N
2459157.97334[a]	23.98	16.08	80
2459182.02270[a]	24.38	30.28	45
2459320.64060[a]	−15.41	18.21	72
2459513.00857[a]	7.44	15.69	83
2459514.00493	25.61	17.30	56
2459515.98987	2.52	14.34	65
2459547.90755	3.92	10.06	91
2459557.00253	24.52	15.63	61
2459564.87333	9.37	13.59	68
2459565.85709	10.60	11.69	80
2459570.84041	0.34	17.46	52
2459572.83906	7.83	17.39	56
2459575.96782	10.38	16.12	59
2459577.94491	−16.59	17.21	55
2459593.77216	−8.50	16.38	58
2459604.88419	3.60	11.49	82
2459626.67754	33.26	21.17	46
2459628.68188[a]	0.75	32.24	46
2459629.68568	−1.94	11.05	85
2459630.68258	10.46	14.14	67
2459631.68481[a]	22.92	24.79	57
2459644.63493	8.00	13.10	72
2459647.64145	−13.73	11.86	82
2459678.67461	18.21	12.85	75
2459680.66011	−24.19	11.09	86
2459683.64781	7.76	10.76	88
2459684.65200	13.47	12.45	76
2459686.64437	−2.79	12.09	79
2459688.62032	−13.99	21.92	45

Note.
[a] Single 15 minute exposure during the nightly visit.

We apply a modified version of the SpEctrum Radial Velocity AnaLyser pipeline (SERVAL; Zechmeister et al. 2018), as outlined in Metcalf et al. (2019), to derive the binned radial velocity (RV) points. To accomplish this, SERVAL combines all observations of TOI-3785 to extract a master spectrum (Anglada-Escudé & Butler 2012) after first identifying and masking telluric and sky emission lines. SERVAL then fits this template to each individual spectrum by shifting it in wavelength space to minimize χ^2. We use the python package barycorrpy (Kanodia & Wright 2018) to further correct for barycentric motion.

We observed TOI-3785 with HPF for 34 visits, with most visits consisting of two 15 minutes exposures per night that were then binned, between 2020 November 4 and 2022 April 19. A median signal-to-noise ratio (S/N) of 69 was calculated at a wavelength of 1070 nm. Of the 34 collected RV points, 29 were kept for the final analysis. Discarded points were done so on the grounds of either unideal weather conditions or significant deviation from the average S/N. Binned RV points along with their errors are listed under Table 2, and the final binned HPF RVs are plotted as dark red points in Figure 3.

2.3.2. NEID

NEID (Halverson et al. 2016; Schwab et al. 2016) is a high-resolution ($R \sim$110,000) spectrograph located on the WIYN 3.5 m telescope at KPNO. NEID covers optical/near-infrared wavelengths ranging from 380 to 930 nm. We observed TOI-3785 between 2021 November 10 and 2022 May 16, obtaining 10 RV points with NEID in high-resolution mode. As NEID allows for longer exposure times than HPF, we obtained a single spectrum per visit with an exposure time of 1800 s, resulting in a median S/N of 15 at 850 nm. The raw spectra were reduced through the NEID Data Reduction Pipeline,[21] and we retrieved the Level-2 2D extracted spectra.[22] We derived RVs using a modified SERVAL pipeline designed specifically for NEID data (Stefànsson et al. 2022). NEID RVs and errors are reported in Table 3 and plotted in gold in Figure 3.

3. Stellar Parameters

We used the HPF spectra and HPF-SpecMatch (Stefansson et al. 2020) to derive the effective temperature ($T_{\rm eff}$), metallicity (Fe/H), $v \sin i$, and $\log g$ priors for the host star, TOI-3785. Based on Yee et al. (2017), HPF-SpecMatch uses a spectral database of well-characterized stellar targets with high S/N HPF observations comparing each star to that of TOI-3785. By creating a composite of library spectra and minimizing the χ^2 of the composite, we obtain best-fit values for each parameter. Uncertainties in the spectroscopic parameters were then determined from cross-validation estimates (for additional details see Stefansson et al. 2020). We estimate the following stellar priors, $T_{\rm eff} = 3576 \pm 88$ K, $\log(g) = 4.747 \pm 0.0458$, and ${\rm Fe/H} = 0.099 \pm 0.117$ (Table 4).

We then estimate the stellar mass, radius, and age by modeling the spectral energy distribution (SED) using the MIST model grids Dotter (2016), Choi et al. (2016) as implemented in the EXOFASTv2 (Eastman et al. 2019) package. The SED fit used Gaussian priors on the (i) 2MASS J, H, K magnitudes (Cutri et al. 2003), PS1 g', r', y' PSF magnitudes from Chambers et al. (2016), Magnier et al. (2020), and Wide-field Infrared Survey Explorer magnitudes (Wright et al. 2010);[23] (ii) spectroscopic parameters derived from HPF-SpecMatch; and (iii) the geometric distance calculated from Bailer-Jones et al. (2021). The upper limit to the visual extinction is determined using estimates of Galactic dust (Green et al. 2019) calculated at the distance determined by Bailer-Jones et al. (2021). The $R_v = 3.1$ reddening law from Fitzpatrick (1999) is employed to convert the extinction from Green et al. (2019) to a visual magnitude extinction. This fit calculates that the host star TOI-3785 has a mass of 0.52 ± 0.02 $M_\odot$, radius of 0.50 ± 0.01 $R_\odot$, luminosity of $0.0367^{+0.0008}_{-0.0009}$ $L_\odot$, and an estimated age of $8.0^{+4.1}_{-4.8}$ Gyr (Table 4). These parameters, combined with the SED derived effective temperature of 3580 ± 47 K, classifies the star as a M2-dwarf spectral-type star (Damiani et al. 2016).

To evaluate the activity of TOI-3785, we examine a Lomb–Scargle periodogram (Lomb 1976) derived from the short cadence TESS light curve. We find no significant peaks corresponding to stellar rotation. We also used the publicly available photometry from the Zwicky Transient Facility (ZTF; Bellm et al. 2019) in the g' and r' filters and the All-Sky Automated Survey for Supernovae (Kochanek et al. 2017) in its V filter. The Lomb–Scargle analysis from both sources again reports no statistically significant rotation signals in the

[21] https://neid.ipac.caltech.edu/docs/NEID-DRP/
[22] https://neid.ipac.caltech.edu/search.php
[23] Stellar magnitudes are listed in Table 1

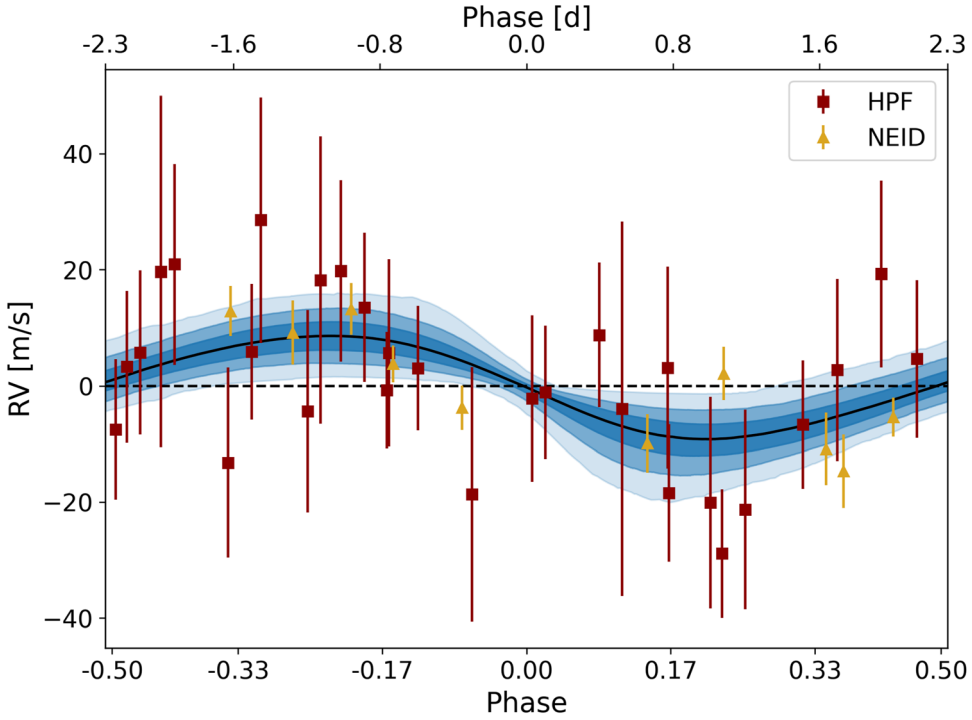

Figure 3. Phase-folded RV points from both HPF (dark red) and NEID (gold) with the best-fit model plotted in blue along with the 1, 2, and 3σ contours (similar to Figure 1) generated from the `exoplanet` joint fit.

Table 3
NEID RV Points

BJD_{TDB}	RV (m s^{-1})	σ (m s^{-1})	S/N
2459529.01052	15.7	5.26	15
2459532.01789	−4.52	3.91	20
2459533.01626	11.74	5.07	16
2459533.91777	12.63	3.69	21
2459538.97354	−9.06	4.43	18
2459569.04250	−9.32	7.27	11
2459586.75088	−8.23	5.89	14
2459619.89833	7.11	5.43	15
2459629.91089	0.82	7.47	11
2459715.67442	18.02	6.51	13

photometry. This lack of detection is expected given our estimated $v \sin i$ is below our detection threshold from `HPF-SpecMatch` (<2 km s^{-1}). We further support this claim by investigating the Calcium Infrared Triplet lines (Mallik 1997; Andretta et al. 2005; Cincunegui et al. 2007; Martin et al. 2017) observed by HPF and Hα lines observed by NEID. No lines exhibited signs of emission, suggesting low activity in the chromosphere of TOI-3785 (Newton et al. 2016). Thus, we conclude that TOI-3785 is a slowly rotating, inactive M2-dwarf star.

4. Analysis

4.1. Data Reduction

We use `AstroImageJ` (Collins et al. 2016) to perform the reductions of TOI-3785's ground-based photometry. For each of the ground-based observations, we subtract a median master bias file, and for the RBO photometry, we additionally subtract a median master dark current file (at short exposure times there is no significant dark current for the ARCTIC observations).

Table 4
TOI-3785 b System Parameters

Parameter	Label (Units)	Value
Orbital parameters:		
RV semiamplitude	K (m s^{-1})	9.24 ± 2.68
Orbital period	P (days)	4.6747373 ± 0.0000038
Transit midpoint	T_0 (BJD)	$2458861.49553^{+0.00060}_{-0.00058}$
Scaled radius	R_p/R_*	0.0962 ± 0.0017
Scaled semimajor axis	a/R_*	$18.89^{+0.45}_{-0.44}$
Impact parameter	b	$0.60^{+0.02}_{-0.03}$
Planetary parameters:		
Eccentricity	e	$0.11^{+0.10}_{-0.08}$ ($2\sigma < 0.26$)
Inclination	i (degrees)	88.1 ± 0.01
Omega	ω (degrees)	$96.26^{+51.25}_{-143.93}$
Transit duration	$T_{\rm Dur}$ (days)	0.071 ± 0.001
Transit depth	$(R_p/R_*)^2$ (ppm)	9254 ± 3
Mass	M_p ($M_\oplus$)	$14.95^{+4.10}_{-3.92}$
Radius	R_p ($R_\oplus$)	5.14 ± 0.16
Density	ρ_p (g/cm^3)	$0.61^{+0.18}_{-0.17}$
Semimajor axis	a (AU)	0.043 ± 0.001
Isolation	S_p ($S_\oplus$)	19.1 ± 2.0
Equilibrium temperature	T_{eq} (K)	582 ± 16
Stellar parameters:		
Mass	M_* ($M_\odot$)	0.52 ± 0.02
Radius	R_* ($R_\odot$)	0.50 ± 0.01
Luminosity	L_* ($L_\odot$)	$0.0367^{+0.0008}_{-0.0009}$
Effective temperature	$T_{\rm eff}$ (Kelvin)	3576 ± 88 K
Surface gravity	$\log g$ (cgs)	4.747 ± 0.0458
Rotational velocity	$v \sin i$ (km s^{-1})	<2
Metallicity	[Fe/H] (dex)	0.099 ± 0.117
Age	(Gyr)	$8.0^{+4.1}_{-4.8}$

Table 5
Photometry/Radial Velocity Correctional Terms

Parameter	Label (Units)	Value			
Photometric parameters:		TESS S20	TESS S47	APO	RBO
Linear limb-darkening coefficient	u_1	$0.36^{+0.39}_{-0.26}$	$0.26^{+0.31}_{-0.19}$	$0.27^{+0.26}_{-0.19}$	$0.35^{+0.43}_{-0.25}$
Quadratic limb-darkening coefficient	u_2	$0.17^{+0.37}_{-0.37}$	$0.14^{+0.32}_{-0.27}$	$0.046^{+0.268}_{-0.214}$	$0.10^{+0.37}_{-0.31}$
Photometric jitter	$\sigma_{\rm phot}$(ppm)	53^{+55}_{-33}	110^{+103}_{-67}	3056^{+98}_{-91}	3830^{+430}_{-360}
Dilution factor	D	$0.97^{+0.06}_{-0.05}$	0.92 ± 0.05	***	***
RV parameters:		HPF	NEID		
RV jitter	$\sigma_{\rm RV}$ (m s^{-1})	$2.9^{+3.1}_{-2.1}$	$7.7^{+3.5}_{-2.6}$		
RV offset	$\gamma_{\rm RV}$ (m s^{-1})	4.7 ± 3.3	1.1 ± 2.9		
RV trend[a]	$\dot{\gamma}$ (mm s^{-1} day^{-1})	$-2.1^{+4.2}_{-4.3}$			
Absolute RV[a]	ΔRV (m s^{-1})	4657 ± 152			

Note.
[a] Not instrument specific

The bias and dark corrected images were then divided by their respective normalized sky flats.

After initial data reductions were completed, we select appropriate aperture sizes for the target and reference stars to minimize both the background noise and any potential stellar interference in our photometry. We then perform differential aperture photometry using `AstroImageJ`, of the primary target and five to seven reference stars assuming a constant aperture size with a radius of 5.48″ and 7.8″ for APO and RBO, respectively. Background values were measured by assuming a median value derived from annuli around each star with an inner and outer radius of 9.12″, 14.6″ for APO and 10.4″, 13.0″ for the RBO data. Uncertainties were calculated by `AstroImageJ` assuming photon noise from the star, background, and dark current (for RBO) and respective read noise for the individual instruments. In post-processing, we found it was unnecessary to detrend the light curves using any external parameters (airmass, background, etc.).

4.2. Joint Fitting

Using the python package `exoplanet` (Foreman-Mackey et al. 2021), we perform a joint fit of all transit photometry (TESS + ARCTIC + RBO) and RV measurements (HPF + NEID). We derived the final transit and radial velocity models in addition to a collection of stellar and planetary parameters that were previously estimated in the `AstroImageJ` fit. Tables 4 and 5 list the finalized transit and system parameters produced by this joint fit.

From the transit observations, we derive a best-fit a/R_*, impact parameter (b), transit depth $(R_p/R_s)^2$, and midtransit ephemeris. We reparameterized and then fit the limb-darkening parameters as suggested in Kipping (2013) to ensure uninformative sampling of quadratic parameters. As each instrument employs a different bandpass, we fit for individual quadratic limb-darkening terms. We also include a photometric noise jitter term added in quadrature to the error bars and the addition of a flux offset value to each light curve.

Due to TESS's large pixel sizes, photometric dilution is a common source of error in transit depth estimations (Sullivan et al. 2015). TESS dilution may cause photometric variation in our reported transit depth causing our errors to inflate. We account for this by fitting a separate dilution term multiplied to the transit depth for each TESS Sector (as described in Bryant et al. 2020)). For TESS Sector 20, we measure a dilution factor of $D_{\rm TESS_{20}} = 0.97^{+0.06}_{-0.05}$ and for TESS Sector 47 a dilution factor of $D_{\rm TESS_{47}} = 0.92 \pm 0.05$. Our high-precision uncontaminated ground-based photometry from ARCTIC (which we use as the baseline fixed to a dilution of 1) enabled us to properly account for this variation.

Figure 1 displays our best-fit photometric transit models. These folded light curves report a transit depth of $0.9254\% \pm 0.0003\%$ and transit duration of $T_{\rm duration} = 0.071 \pm 0.001$ days ($\sim$1.7 hr). Each transit plot presents a 10 minute bin of the reduced data and residuals as well as values of median photometric error.

For the radial velocity observations, we include linear RV trend terms for both HPF and NEID to account for any slight positive or negative slopes in the RVs caused by instrumental drift. In addition, we report the instrument-specific factors of RV jitter and offset. The jitter term is used to estimate the degree of RV error inflation in order to meet an expected RV fit. All photometric and radial velocity correction terms are reported in Table 5. We plot, in Figure 3, the `exoplanet` RV fit including all HPF and NEID points. The best-fit model indicates an RV semiamplitude of 9.24 ± 2.68 m s^{-1} and an eccentricity of $e = 0.11^{+0.10}_{-0.08}$. From this analysis, we determine that TOI-3785 b has a radius of $5.14 \pm 0.16\,R_\oplus$ and a mass of $14.95^{+4.10}_{-3.92}\,M_\oplus$. Table 4 lists the finalized planetary and orbital parameters produced by this joint fit.

4.3. Planetary Companions

Further analyzing the transit data, we search for additional periodic signals by implementing a box least squared (BLS; Kovács et al. 2002) algorithm of all available TESS data extracted from the MAST archive (MAST Team 2021). The known transit of TOI-3785 b in both Sectors 20 and 47 were masked to twice the duration in order to search for other potential period detections that may indicate additional transiting planets in the TOI-3785 system. The masked BLS periodograms report no significant peaks over the false alarm probability (FAP) of 10%.

Additionally, periodograms of HPF and NEID also show no additional significant peaks (stellar or planetary in nature). The existing data does not reveal the presence of a close-period companion in this system as the known signal of TOI-3785 b recovers the lowest FAP at 10%. However, the limited

coverage of this system with both TESS and RV monitoring cannot rule out the potential for additional long-period planets. From our available transit and RV data, we see no detection of additional orbiters, but a more in-depth analysis is required for a concrete claim to be made.

5. Discussion

5.1. TOI-3785 b in Parameter Space

In order to emphasize the unique planetary characteristics of TOI-3785 b we compare this system to other confirmed exoplanet targets in Figure 4. We plot TOI-3785 b in both planetary mass–radius (Figure 4; top) and $T_{\rm eff}$–radius (Figure 4; bottom) space. These systems were compiled from the NASA Exoplanet Archive (Akeson et al. 2013) as of 2023 March 1 using the following parameter constraints: an upper planetary radius limit of 14 $R_\oplus$ and a radius and mass significance cut off at $>3\sigma$. For the mass–radius plot we limit the stellar effective temperature to <4000 K (the upper temperature boundary of M dwarfs; Casagrande et al. 2008) and include planetary density contour lines at 0.5, 1, 3, and 10 g cm^{-3}.

The parameter spaces of Figure 4 both show TOI-3785 b, indicated by a blue circle, to be a meaningful addition to the current number of known M-dwarf-hosted targets. Due to its planetary radius , TOI-3785 b occupies the rare M-dwarf Neptune population (4 $R_\oplus < R_p < 7$ $R_\oplus$) of which only eight others have been confirmed with a $>3\sigma$ mass and radius (Figure 4). This dearth in the Neptune population becomes clear when the vast number of lower radii targets ($<3R_\oplus$) is considered. It is widely known that lower mass M dwarfs have a higher occurrence rate for smaller (and likely terrestrial in composition) close-in planets with Dressing & Charbonneau (2013) discovering a sharp decrease in occurrence rate at 4 $R_\oplus$.

The M-dwarf Jupiter population (>7 $R_\oplus$) is seen to be relatively sparse compared to FGK occurrence totaling only ~15 mass significant targets. M-dwarf Jupiters do not come close to rivaling the M-dwarf Earth population (<3 $R_\oplus$) in which ~35 $>3\sigma$ mass targets are known. Still, first approximations of occurrence rates have been derived for close-in Jupiters orbiting M dwarfs, even with this small sample size (~1%; Bryant et al. 2023; Gan et al. 2023). However, the occurrence of M-dwarf Neptunes (4 $< R_p <$ 7 $R_\oplus$) has yet to be the focus of a targeted study—in part due to the <10 confirmed detections. TESS's focus on nearby M dwarfs is steadily growing the Neptune population. With the discovery of additional Neptunes similar to TOI-3785 b, we may soon derive the first occurrence rates for Neptunes and move closer toward a complete picture regarding the occurrence of all M-dwarf populations.

5.2. Constraints on M-dwarf Planetary Formation

The leading theory of Neptune formation around M dwarfs is core accretion (Laughlin et al. 2004), in which the formation of a solid core generates a disk of gas and dust from surrounding debris that is slowly accreted onto the surface of the protoplanet. In cases of ample material and undisturbed mass accumulation, a protoplanet may reach a critical mass triggering runaway accretion in which a planet's mass exponentially increases. This is the traditional formation pathway for many Jupiter mass planets (e.g., Bodenheimer & Pollack 1986; Pollack et al. 1996). In the case of the less massive Neptune population, there must be an inhibitor to prevent runaway accretion from taking place: either the protoplanet lacks sufficient material to accrete onto its surface or it lacks sufficient time to grow to a critical mass (Deleuil et al. 2020). Laughlin et al. (2004) argues that due to the smaller M-dwarf disk masses, gas giant cores require additional time to form. If they reach the critical mass threshold to begin accumulating H/He, their runaway growth stage is cut short due to disk dispersion.

TOI-3785 b appears to support this formation theory. Using the Exoplanet Compositional Interpolator[24] based on models from Lopez & Fortney (2014), we estimate a H/He mass fraction of 20% (~3 $M_\oplus$) with a heavy-element (core) mass fraction of 80% (11.95 $M_\oplus$) for TOI-3785 b. As this is slightly more massive than the predicted core mass required for runaway accretion, we conclude that TOI-3785 b's core must have formed slowly following the predicted pathway highlighted in Laughlin et al. (2004). With 20% of its mass in a H/He envelope, it appears TOI-3785 b was poised to begin runaway accretion. However, this accretion stalled potentially due to the disk dispersing or the planet migrating inwards to its present-day location. By further investigating TOI-3785 b's composition, we may constrain the formation timeline of M-dwarf hosting Neptunes to derive reasonable evolutionary pathways for these rare targets.

5.3. The Neptune Desert

The Neptune desert is a region of parameter space in which remarkably few Neptune-sized targets have been confirmed around FGK stars. Targets that inhabit this region are defined by their Neptune radii as well as low orbital periods and high insolations. TOI-3785 b lies within the Neptune-desert regime as defined in radius–period space in Mazeh et al. (2016; Figure 5; top). However, the bounds of this desert were derived from FGK targets confirmed by the Kepler mission. M-dwarf targets, such as TOI-3785 b, may have misleading placements within the desert as low-temperature stars will produce planets with low insolation even at short periods. TOI-3785 b possesses a short orbital period of 4.67 days and its cooler host star yields a significantly smaller insolation (19× Earth Insolation) when compared to planets around FGK stars that normally yield insolations within the range of 100–1000 $S_\oplus$. Therefore, the Neptune Desert should be considered in radius-insolation space for M-dwarf hosting systems. TOI-3785 b sits outside of the Insolation Neptune Desert space as defined by Kanodia et al. (2021; Figure 5; bottom).

TOI-532 b (Kanodia et al. 2021) is a similarly-sized planet compared to TOI-3785 b orbiting a slightly larger M0 dwarf. TOI-532 b is also the only M-dwarf Neptune that possesses a large enough insolation (94 $S_\oplus$) to be considered within the FGK bounds of the insolation Neptune Desert. While similarly sized, this planet possesses a substantially higher mass and density than all other M-dwarf Neptunes suggesting it experienced significant H/He escape during its lifetime. With its low insolation, TOI-3785 b likely experienced little to no atmospheric escape during its evolution.

5.4. Atmospheric Comparative Planetology

TOI-3785 b joins the growing list of promising targets for atmospheric characterization (Table 6). We calculate its

[24] https://tools.emac.gsfc.nasa.gov/ECI/

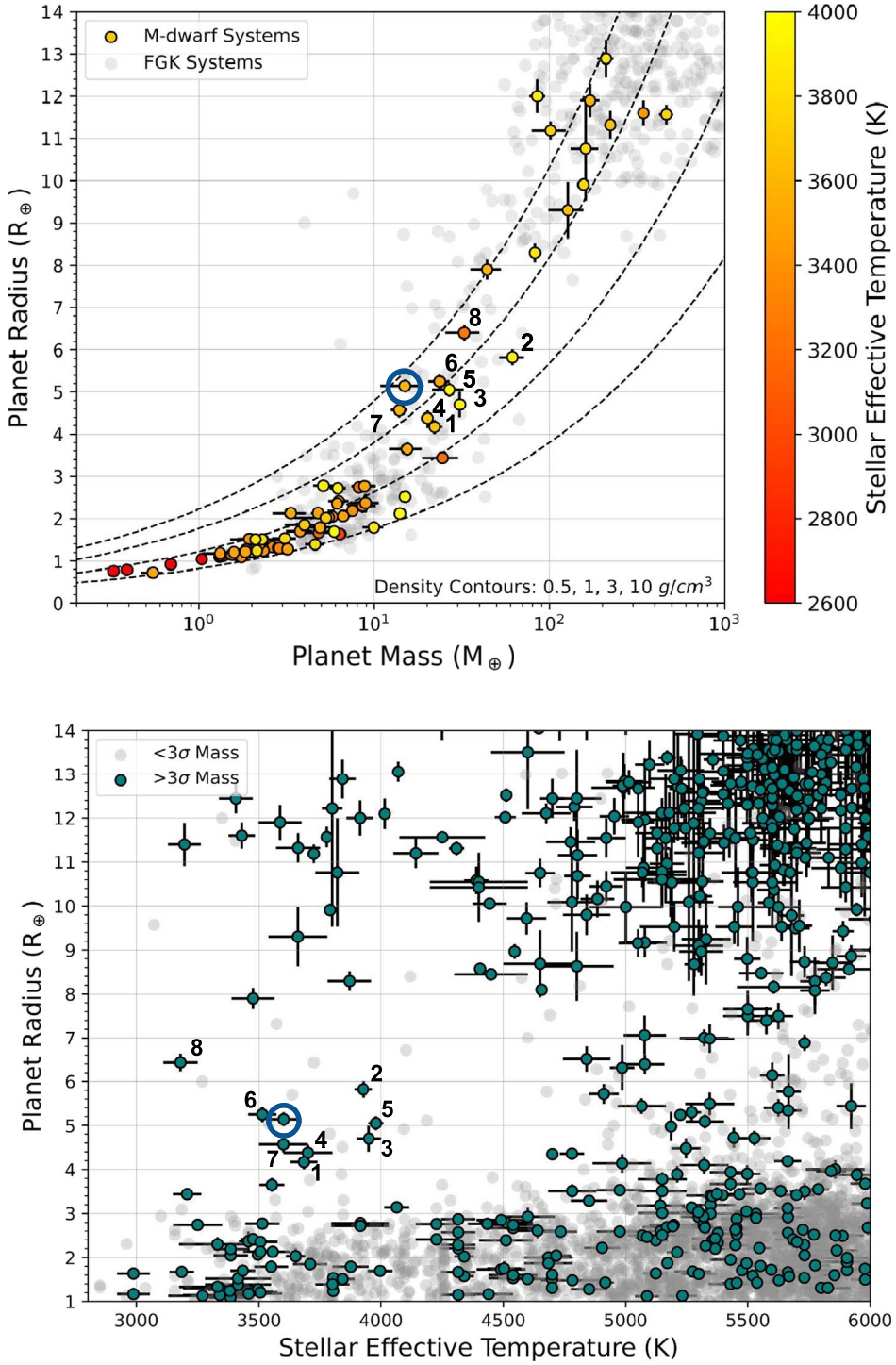

Figure 4. Top: planet radius against planet mass of only M-dwarf targets (restricted by an upper bound on effective temperature of $T_{\rm eff} < 4000$K). The points with attributed effective temperatures are M-dwarf planets that have $>3\sigma$ mass precision. Gray points represent $>3\sigma$ FGK targets. The dashed lines are density contours with specific values listed in the bottom right. Bottom: planetary radius against stellar effective temperature, to place TOI-3785 b against a broader range of stellar host types. Colored points represent $>3\sigma$ mass precision while targets under this threshold are grayed out. We also highlight the lack of planetary confirmation between (4000 K $< T_{\rm eff} <$ 4700 K). This is most likely a result of the shallow transit depths that are characteristic of K-dwarf stars. This creates a detection bias as K-dwarf planets produce weaker transiting signals. In both figures, similar M-dwarf Neptunes to TOI-3785 b are labeled and listed in Table 6.

transmission spectroscopy metric (TSM) following Equation (1) in Kempton et al. (2018) finding a TSM value of 147 (Figure 6). TOI-3785 b possesses one of the highest TSMs for any planet cooler than 600 K–with AU Mic b the only other planet in this temperature regime with a higher TSM. Since AU Mic is an active star (Plavchan et al. 2020), difficulties probing AU Mic b's atmosphere may arise due to stellar interference. Thus, the inactivity of TOI-3785 b's host star makes it the best target for exploring this temperature regime.

TOI-3785 b also possesses similar planetary and stellar parameters as two Neptunes with well-characterized transmission spectra: GJ 3470 b (e.g., Crossfield et al. 2013; Ehrenreich et al. 2014; Dragomir et al. 2015) and GJ 436 b (e.g., Knutson et al. 2014). Both of these targets possess featureless spectra

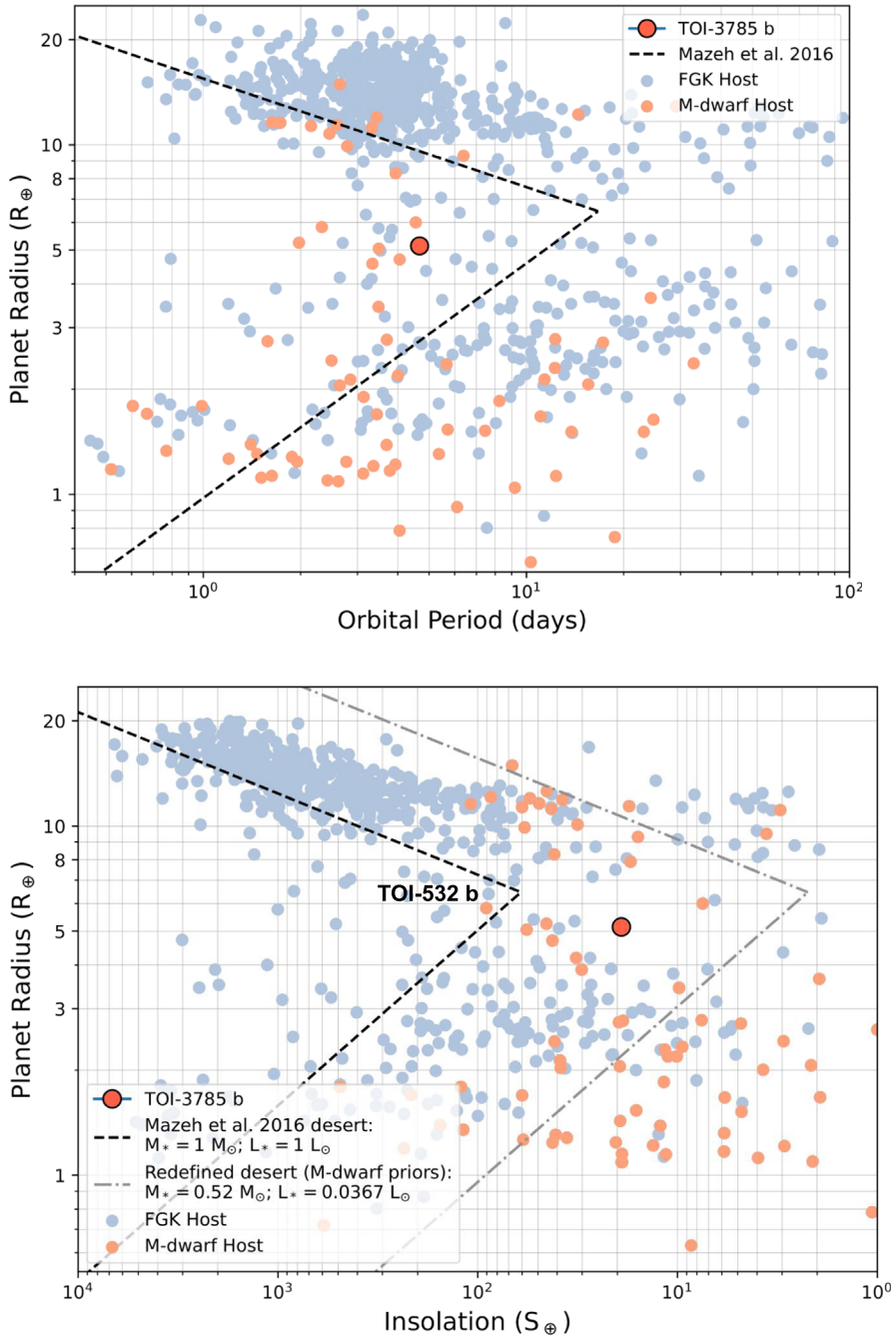

Figure 5. Top: the Neptune Desert as reported by Mazeh et al. (2016) in orbital period—planetary radius space. Indicated by the red dot is TOI-3785 b. Bottom: we reorient the Neptune Desert bounds to apply to insolation—radius space as per host star characteristics. The dark lines represent the desert for Sun-like stars that define appropriate bounds for FGK hosts. The gray lines show a redefined desert that considers the lower mass and luminosity of M-dwarf hosts, so much so that this boundary is no longer defined as a notable desert. If we instead use the insolation-based definition (black dashed line), only one planet around an M dwarf, TOI-532 b (see Table 6), falls inside the Neptune Desert. In both cases, only $>3\sigma$ mass targets are considered.

within Hubble's Wide Field Camera 3 bandpass (1.1–1.7 μm) indicating hazy atmospheres; a characteristic that TOI-3785 b could share (Yu et al. 2021; Dymont et al. 2022). By leveraging JWST's NIRSpec-Prism longer wavelength coverage, the hazes should become translucent at wavelengths beyond 3 microns allowing for both characterization of the haze layer and the atmospheric composition beneath (Kawashima et al. 2019). TOI-3785 b therefore presents an opportunity to not only explore the atmosphere of a warm-Neptune but also enable insightful atmospheric comparisons with similar planets around similar stars. Interestingly, both GJ 3470 b and GJ 436 b have escaping atmospheres observed via helium (for GJ 3470b Ninan et al. 2020) or Lyα (for GJ 436 b Ehrenreich et al. 2015) absorption features. TOI-3785 b's low density of $\sim$0.6 g cm^{-3} along with similarities between this system and GJ 3470 (stellar parameters) makes it a promising target for helium follow up.

6. Summary

Using both ground-based and TESS transit photometry as well as spectroscopic RV follow up of the TOI-3785 system, we confirm the existence of a single planetary companion, TOI-3785 b, a warm-Neptune with a 4.67 days circular orbit around

Table 6
Similar M-dwarf Neptune Targets Ordered by Planet Density

Planet / Source	$T_{\rm eff}$ (K)	TSM	$T_{\rm EQ}$ (K)	S_p ($S_\oplus$)	M_p ($M_\oplus$)	R_p ($R_\oplus$)	ρ_p (g cm^{-3})
[1] GJ 436 b Maciejewski et al. (2014)	3586 ± 36	453	686 ± 10	41 ± 4	22.1 ± 2.3	4.170 ± 0.168	1.80 ± 0.29
[2] TOI-532 b Kanodia et al. (2021)	3927 ± 37	43	867 ± 18	94.10 ± 8.00	$61.5^{+9.7}_{-9.3}$	5.82 ± 0.19	1.72 ± 0.31
[3] LP 714-47 b Dreizler et al. (2020)	3950 ± 51	140	700^{+19}_{-24}	46 ± 2	30.8 ± 1.5	4.7 ± 0.3	1.7 ± 0.3
[4] AU Mic b[a] Plavchan et al. (2020)	3700 ± 100	414	$569.5^{+5.1}_{-4.5}$	22 ± 2	$20.12^{+1.57}_{-1.72}$	4.38 ± 0.18	$1.32^{+0.19}_{-0.20}$
[5] TOI-1728 b Kanodia et al. (2020)	3980 ± 32	130	767 ± 8	57.78 ± 3.48	$26.78^{+5.43}_{-5.13}$	$5.05^{+0.16}_{-0.17}$	$1.14^{+0.26}_{-0.24}$
[6] TOI-674 b Murgas et al. (2021)	3514 ± 57	215	635 ± 15	38.4 ± 0.1	23.6 ± 3.3	5.25 ± 0.17	0.91 ± 0.15
[7] GJ 3470 b Awiphan et al. (2016)	3622^{+58}_{-55}	272	615 ± 16	42 ± 6	13.9 ± 1.5	4.57 ± 0.18	0.80 ± 0.13
[8] TOI-3884 b[a] Almenara et al. (2022) Libby-Roberts et al. (2023)	3180 ± 88	230	441 ± 15	6.29 ± 0.84	$32.59^{+7.31}_{-7.38}$	6.43 ± 0.20	$0.67^{+0.18}_{-0.16}$
TOI-3785 b This work	3576 ± 88	147	582 ± 16	19.1 ± 2.0	$14.95^{+4.10}_{-3.92}$	5.14 ± 0.16	$0.61^{+0.18}_{-0.17}$

Note.
[a] Active host star.

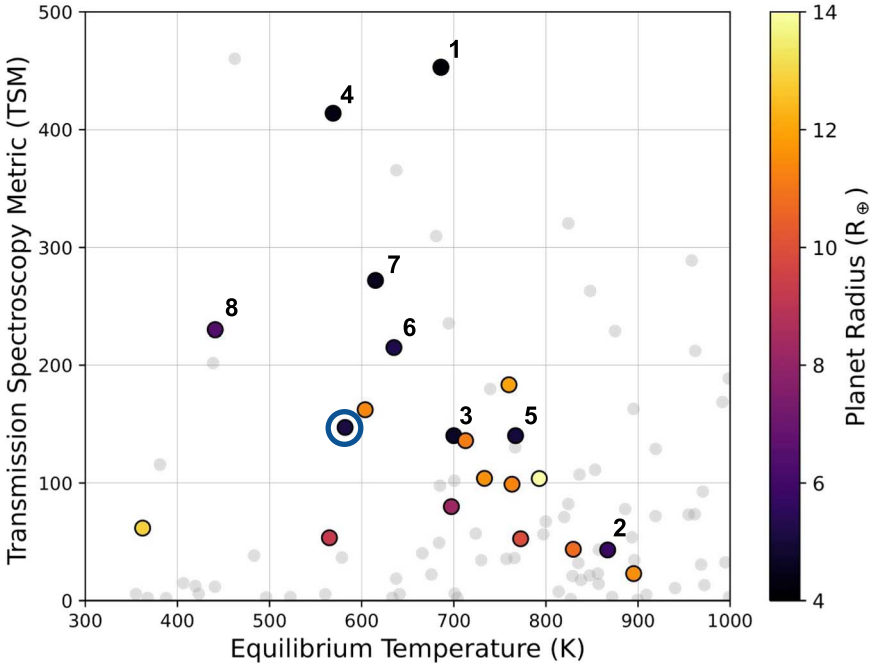

Figure 6. The TSM of known exoplanets with both a measured ($>3\sigma$) mass and radii $>4\ R_\oplus$ as a function of equilibrium temperature. Planets orbiting M dwarfs are labeled according to Table 6 and are noted with colors varying by their respective planetary radii, while planets orbiting FGK-dwarf stars are plotted as gray points. TOI-3785 b (navy blue circle) possesses one of the highest TSMs for any planet cooler than 600 K, making it a promising target for future transmission spectroscopy observations.

an M2V-dwarf star. Using the package `exoplanet` we model both the transit observations and RVs to derive a planetary mass of $14.95^{+4.10}_{-3.92} M_\oplus$ and radius of $5.14 \pm 0.16 R_\oplus$. The confirmation of TOI-3785 b proves to be a valuable addition to the small number of M-dwarf-hosted Neptunes as increased target confirmation in this space may support Neptune formation models such as the joint efforts of core accretion and situational disk dispersion. Future investigations into this target via transmission spectroscopy are warranted as it possesses an ideal TSM along with favorable constraints on atmospheric hazing. The noteworthy similarities to GJ 3470 b and GJ 436 b may also demonstrate similarly influential results on the composition and formation pathways of M-dwarf gas planets. Furthermore, we discuss TOI-3785 b's place relative to the radius–period and radius-insolation Neptune Deserts and the necessary cautions that accompany M-type hosts and desert classifications.

Acknowledgments

We want to thank the anonymous referee for their thoughtful suggestions and time spent on this work. Their comments regarding the specifics of planetary occurrence and Neptune detection were helpful in shaping the discussion of this

planetary target. The Center for Exoplanets and Habitable Worlds is supported by Penn State and the Eberly College of Science. Computations for this research were performed on the Penn State's Institute for Computational and Data Sciences' Advanced Cyber Infrastructure (ICDS-ACI). This content is solely the responsibility of the authors and does not necessarily represent the views of the Institute for Computational and Data Sciences. The Pennsylvania State University campuses are located on the original homelands of the Erie, Haudenosaunee (Seneca, Cayuga, Onondaga, Oneida, Mohawk, and Tuscarora), Lenape (Delaware Nation, Delaware Tribe, Stockbridge-Munsee), Shawnee (Absentee, Eastern, and Oklahoma), Susquehannock, and Wahzhazhe (Osage) Nations. As a land grant institution, we acknowledge and honor the traditional caretakers of these lands and strive to understand and model their responsible stewardship. We also acknowledge the longer history of these lands and our place in that history.

W.D.C. acknowledges support from NSF grant AST 2108801.

These results are based on observations obtained with the Habitable-zone Planet Finder Spectrograph on the HET. We acknowledge support from NSF grants AST-1006676, AST-1126413, AST-1310885, AST-1310875, AST-1910954, AST-1907622, AST-1909506, ATI 2009889, ATI-2009982, AST-2108512, and the NASA Astrobiology Institute (NNA09-DA76A) in the pursuit of precision radial velocities in the NIR. The HPF team also acknowledges support from the Heising-Simons Foundation via grant 2017-0494. The Hobby–Eberly Telescope is a joint project of the University of Texas at Austin, the Pennsylvania State University, Ludwig-Maximilians-Universität München, and Georg-August Universität Gottingen. The HET is named in honor of its principal benefactors, William P. Hobby and Robert E. Eberly. The HET collaboration acknowledges the support and resources from the Texas Advanced Computing Center. We thank the Resident Astronomers and Telescope Operators at the HET for the skillful execution of our observations with HPF. We would like to acknowledge that the HET is built on Indigenous land. Moreover, we would like to acknowledge and pay our respects to the Carrizo & Comecrudo, Coahuiltecan, Caddo, Tonkawa, Comanche, Lipan Apache, Alabama-Coushatta, Kickapoo, Tigua Pueblo, and all the American Indian and Indigenous Peoples and communities who have been or have become a part of these lands and territories in Texas, here on Turtle Island.

Based on observations at Kitt Peak National Observatory, NSF's NOIRLab, managed by the Association of Universities for Research in Astronomy (AURA) under a cooperative agreement with the National Science Foundation. The authors are honored to be permitted to conduct astronomical research on Iolkam Du'ag (Kitt Peak), a mountain with particular significance to the Tohono O'odham. Deepest gratitude to Zade Arnold, Joe Davis, Michelle Edwards, John Ehret, Tina Juan, Brian Pisarek, Aaron Rowe, Fred Wortman, the Eastern Area Incident Management Team, and all of the firefighters and air support crew who fought the recent Contreras fire. Against great odds, you saved Kitt Peak National Observatory.

Data presented herein were obtained at the WIYN Observatory from telescope time allocated to NN-EXPLORE through the scientific partnership of the National Aeronautics and Space Administration, the National Science Foundation, and the National Optical Astronomy Observatory. WIYN is a joint facility of the University of Wisconsin-Madison, Indiana University, NSF's NOIRLab, the Pennsylvania State University, Purdue University, University of California, Irvine, and the University of Missouri.

Data presented were obtained by the NEID spectrograph built by Penn State University and operated at the WIYN Observatory by NSF's NOIRLab, under the NN-EXPLORE partnership of the National Aeronautics and Space Administration and the National Science Foundation. This work was performed for the Jet Propulsion Laboratory, California Institute of Technology, sponsored by the United States Government under the Prime Contract 80NM0018D0004 between Caltech and NASA. These results are based on observations obtained with NEID under proposals 2021B-0035 (PI: S. Kanodia), 2021B-0435 (PI: S. Kanodia), 2022A-452266 (PI: S. Kanodia), and 2022A-794607 (PI: J. Libby-Roberts). We thank the NEID Queue Observers and WIYN Observing Associates for their skillful execution of our NEID observations.

Some of the observations in this paper made use of the NN-EXPLORE Exoplanet and Stellar Speckle Imager (NESSI). NESSI was funded by the NASA Exoplanet Exploration Program and the NASA Ames Research Center. NESSI was built at the Ames Research Center by Steve B. Howell, Nic Scott, Elliott P. Horch, and Emmett Quigley.

The WIYN Observatory is a joint facility of the NSF's National Optical-Infrared Astronomy Research Laboratory, Indiana University, the University of Wisconsin-Madison, Pennsylvania State University, the University of Missouri, the University of California–Irvine, and Purdue University. The ground-based photomety is based on observations obtained with the Apache Point Observatory 3.5 m telescope, which is owned and operated by the Astrophysical Research Consortium. We acknowledge support from NSF grant AST-1907622 in the pursuit of precise photometric observations from the ground.

Based on observations obtained with the Samuel Oschin 48 inch Telescope at the Palomar Observatory as part of the Zwicky Transient Facility project. Z.T.F. is supported by the National Science Foundation under Grant No. AST-1440341 and a collaboration including Caltech, IPAC, the Weizmann Institute for Science, the Oskar Klein Center at Stockholm University, the University of Maryland, the University of Washington, Deutsches Elektronen-Synchrotron and Humboldt University, Los Alamos National Laboratories, the TANGO Consortium of Taiwan, the University of Wisconsin at Milwaukee, and Lawrence Berkeley National Laboratories. Operations are conducted by COO, IPAC, and UW.

This research has made use of the SIMBAD database, operated at CDS, Strasbourg, France, and NASA's Astrophysics Data System Bibliographic Services. This research has made use of the Exoplanet Follow-up Observation Program website, which is operated by the 1197 California Institute of Technology, under contract with the National Aeronautics and Space Administration under the Exoplanet Exploration Program. This research has made use of the NASA Exoplanet Archive, which is operated by Caltech, under contract with NASA under the Exoplanet Exploration Program.

Some of the data presented in this manuscript were obtained from the Mikulski Archive for Space Telescopes (MAST) at the Space Telescope Science Institute. The specific observations analyzed can be accessed via (MAST Team 2021; TESS Light Curves—All Sectors).

Some of the data presented in this paper were obtained from MAST at STScI. Support for MAST for non-HST data is provided by the NASA Office of Space Science via grant NNX09AF08G and by other grants and contracts. This work includes data collected by the TESS mission, which are publicly available from MAST. Funding for the TESS mission is provided by the NASA Science Mission directorate.

This work presents results from the European Space Agency (ESA) space mission Gaia. Gaia data are being processed by the Gaia Data Processing and Analysis Consortium (DPAC). Funding for the DPAC is provided by national institutions, in particular the institutions participating in the Gaia MultiLateral Agreement (MLA). The Gaia mission website is https://www.cosmos.esa.int/gaia. The Gaia archive website is https://archives.esac.esa.int/gaia.

This research has made use of the Exoplanet Follow-up Observation Program (ExoFOP, NExScI 2022) website, which is operated by the California Institute of Technology, under contract with the National Aeronautics and Space Administration under the Exoplanet Exploration Program.

C.I.C. acknowledges support by NASA Headquarters through an appointment to the NASA Postdoctoral Program at the Goddard Space Flight Center, administered by USRA through a contract with NASA and the NASA Earth and Space Science Fellowship Program through grant 80NSSC18K1114.

Facilities: TESS, APO (ARCTIC), RBO, Gaia, HET (HPF), WIYN (NEID), NESSI.

ORCID iDs

Luke C. Powers https://orcid.org/0000-0002-5300-5353
Jessica Libby-Roberts https://orcid.org/0000-0002-2990-7613
Andrea S. J. Lin https://orcid.org/0000-0002-9082-6337
Caleb I. Cañas https://orcid.org/0000-0003-4835-0619
Shubham Kanodia https://orcid.org/0000-0001-8401-4300
Suvrath Mahadevan https://orcid.org/0000-0001-9596-7983
Joe P. Ninan https://orcid.org/0000-0001-8720-5612
Guðmundur Stefánsson https://orcid.org/0000-0001-7409-5688
Arvind F. Gupta https://orcid.org/0000-0002-5463-9980
Sinclaire Jones https://orcid.org/0000-0002-7227-2334
Henry A. Kobulnicky https://orcid.org/0000-0002-4475-4176
Andrew Monson https://orcid.org/0000-0002-0048-2586
Brock A. Parker https://orcid.org/0000-0001-9307-8170
Tera N. Swaby https://orcid.org/0000-0002-5817-202X
Chad F. Bender https://orcid.org/0000-0003-4384-7220
William D. Cochran https://orcid.org/0000-0001-9662-3496
Leslie Hebb https://orcid.org/0000-0003-1263-8637
Andrew J. Metcalf https://orcid.org/0000-0001-5000-1018
Paul Robertson https://orcid.org/0000-0003-0149-9678
Christian Schwab https://orcid.org/0000-0002-4046-987X
John Wisniewski https://orcid.org/0000-0001-9209-1808
Jason T. Wright https://orcid.org/0000-0001-6160-5888

References

Akeson, R. L., Chen, X., Ciardi, D., et al. 2013, PASP, 125, 989
Almenara, J. M., Bonfils, X., Forveille, T., et al. 2022, A&A, 667, L11
Andretta, V., Busà, I., Gomez, M. T., & Terranegra, L. 2005, A&A, 430, 669
Anglada-Escudé, G., & Butler, R. P. 2012, ApJS, 200, 15
Awiphan, S., Kerins, E., Pichadee, S., et al. 2016, MNRAS, 463, 2574
Bailer-Jones, C. A. L., Rybizki, J., Fouesneau, M., Demleitner, M., & Andrae, R. 2021, AJ, 161, 147
Bellm, E. C., Kulkarni, S. R., Graham, M. J., et al. 2019, PASP, 131, 018002
Bodenheimer, P., & Pollack, J. B. 1986, Icar, 67, 391
Borucki, W. J., Koch, D., Basri, G., et al. 2010, Sci, 327, 977
Bryant, E. M., Bayliss, D., Nielsen, L. D., et al. 2020, MNRAS, 499, 3139
Bryant, E. M., Bayliss, D., & Van Eylen, V. 2023, MNRAS, 521, 3663
Caldwell, D. A., Tenenbaum, P., Twicken, J. D., et al. 2020, RNAAS, 4, 201
Cañas, C. I., Kanodia, S., Bender, C. F., et al. 2022, AJ, 164, 50
Cañas, C. I., Stefansson, G., Kanodia, S., et al. 2020, AJ, 160, 147
Lightkurve Collaboration, Cardoso, J. V. d. M., Hedges, C., et al. 1812, Lightkurve: Kepler and TESS time series analysis in Python, Astrophysics Source Code Library, ascl:1812.013
Casagrande, L., Flynn, C., & Bessell, M. 2008, MNRAS, 389, 585
Chambers, K. C., Magnier, E. A., Metcalfe, N., et al. 2016, arXiv:1612.05560
Choi, J., Dotter, A., Conroy, C., et al. 2016, ApJ, 823, 102
Cincunegui, C., Díaz, R. F., & Mauas, P. J. D. 2007, A&A, 469, 309
Collins, K. A., Kielkopf, J. F., Stassun, K. G., & Hessman, F. V. 2016, arXiv:1601.02622
Crossfield, I. J. M., Barman, T., Hansen, B. M. S., & Howard, A. W. 2013, A&A, 559, A33
Cutri, R. M., Skrutskie, M. F., van Dyk, S., et al. 2003, The IRSA 2MASS All-Sky Point Source Catalog (Washington, DC: NASA)
Damiani, C., Meunier, J. C., Moutou, C., et al. 2016, A&A, 595, A95
Deleuil, M., Pollacco, D., Baruteau, C., Rauer, H., & Blanc, M. 2020, SSRv, 216, 105
Dotter, A. 2016, ApJS, 222, 8
Dragomir, D., Benneke, B., Pearson, K. A., et al. 2015, ApJ, 814, 102
Dreizler, S., Crossfield, I. J. M., Kossakowski, D., et al. 2020, A&A, 644, A127
Dressing, C. D., & Charbonneau, D. 2013, ApJ, 767, 95
Dymont, A. H., Yu, X., Ohno, K., et al. 2022, ApJ, 937, 90
Eastman, J. D., Rodriguez, J. E., Agol, E., et al. 2019, arXiv:1907.09480
Ehrenreich, D., Bonfils, X., Lovis, C., et al. 2014, A&A, 570, A89
Ehrenreich, D., Bourrier, V., Wheatley, P. J., et al. 2015, Natur, 522, 459
Fitzpatrick, E. L. 1999, PASP, 111, 63
Foreman-Mackey, D., Luger, R., Agol, E., et al. 2021, JOSS, 6, 3285
Gaia Collaboration, Vallenari, A., Brown, A. G. A., et al. 2022, arXiv:2208.00211
Gan, T., Wang, S. X., Wang, S., et al. 2023, AJ, 165, 17
Green, G. M., Schlafly, E., Zucker, C., Speagle, J. S., & Finkbeiner, D. 2019, ApJ, 887, 93
Halverson, S., Terrien, R., Mahadevan, S., et al. 2016, Proc. SPIE, 9908, 99086P
Hill, G. J., Lee, H., MacQueen, P. J., et al. 2021, AJ, 162, 298
Huang, C. X., Vanderburg, A., Pál, A., et al. 2020, RNAAS, 4, 204
Huehnerhoff, J., Ketzeback, W., Bradley, A., et al. 2016, Proc. SPIE, 9908, 99085H
Jenkins, J. M., Twicken, J. D., McCauliff, S., et al. 2016, Proc. SPIE, 9913, 99133E
Kanodia, S., Cañas, C. I., Stefansson, G., et al. 2020, ApJ, 899, 29
Kanodia, S., Mahadevan, S., Ramsey, L. W., et al. 2018, Proc. SPIE, 10702, 107026Q
Kanodia, S., Stefansson, G., Cañas, C. I., et al. 2021, AJ, 162, 135
Kanodia, S., & Wright, J. 2018, RNAAS, 2, 4
Kasper, D. H., Ellis, T. G., Yeigh, R. R., et al. 2016, PASP, 128, 105005
Kawashima, Y., Hu, R., & Ikoma, M. 2019, ApJL, 876, L5
Kempton, E. M. R., Bean, J. L., Louie, D. R., et al. 2018, PASP, 130, 114401
Kipping, D. M. 2013, MNRAS, 435, 2152
Knutson, H. A., Benneke, B., Deming, D., & Homeier, D. 2014, Natur, 505, 66
Kochanek, C. S., Shappee, B. J., Stanek, K. Z., et al. 2017, PASP, 129, 104502
Kovács, G., Zucker, S., & Mazeh, T. 2002, A&A, 391, 369
Laughlin, G., Bodenheimer, P., & Adams, F. C. 2004, ApJL, 612, L73
Libby-Roberts, J. E., Schutte, M., Hebb, L., et al. 2023, arXiv:2302.04757
Lomb, N. R. 1976, Ap&SS, 39, 447
Lopez, E. D., & Fortney, J. J. 2014, ApJ, 792, 1
Maciejewski, G., Niedzielski, A., Nowak, G., et al. 2014, AcA, 64, 323
Magnier, E. A., Schlafly, E. F., Finkbeiner, D. P., et al. 2020, ApJS, 251, 6
Mahadevan, S., Ramsey, L., Bender, C., et al. 2012, Proc. SPIE, 8446, 84461S
Mahadevan, S., Ramsey, L. W., Terrien, R., et al. 2014, Proc. SPIE, 9147, 91471G
Mallik, S. V. 1997, A&AS, 124, 359
Martin, J., Fuhrmeister, B., Mittag, M., et al. 2017, A&A, 605, A113
MAST Team 2021, TESS Light Curves—All Sectors, STScI/MAST, doi:10.17909/T9-NMC8-F686

Mazeh, T., Holczer, T., & Faigler, S. 2016, A&A, 589, A75
Metcalf, A. J., Anderson, T., Bender, C. F., et al. 2019, Optica, 6, 233
Murgas, F., Astudillo-Defru, N., Bonfils, X., et al. 2021, A&A, 653, A60
Newton, E. R., Irwin, J., Charbonneau, D., et al. 2016, in 19th Cambridge Workshop on Cool Stars, Stellar Systems, and the Sun (CS19) (Cambridge: Cambridge Univ. Press), 4
NExScI 2022, Exoplanet Follow-up Observing Program Web Service, IPAC, doi:10.26134/EXOFOP5
Ninan, J. P., Bender, C. F., Mahadevan, S., et al. 2018, Proc. SPIE, 10709, 107092U
Ninan, J. P., Stefansson, G., Mahadevan, S., et al. 2020, ApJ, 894, 97
Plavchan, P., Barclay, T., Gagné, J., et al. 2020, Natur, 582, 497
Pollack, J. B., Hubickyj, O., Bodenheimer, P., et al. 1996, Icar, 124, 62
Ramsey, L. W., Adams, M. T., Barnes, T. G., et al. 1998, Proc. SPIE, 3352, 34
Ricker, G. R., Winn, J. N., Vanderspek, R., et al. 2015, JATIS, 1, 014003
Schwab, C., Rakich, A., Gong, Q., et al. 2016, Proc. SPIE, 9908, 99087H
Scott, N. J., Howell, S. B., Horch, E. P., et al. 2018, PASP, 130, 054502
Stefansson, G., Cañas, C., Wisniewski, J., et al. 2020, AJ, 159, 100
Stefansson, G., Hearty, F., Robertson, P., et al. 2016, ApJ, 833, 175
Stefansson, G., Mahadevan, S., Hebb, L., et al. 2017, ApJ, 848, 9
Stefànsson, G., Mahadevan, S., Petrovich, C., et al. 2022, ApJL, 931, L15
Stefansson, G., Mahadevan, S., Wisniewski, J., et al. 2018, Proc. SPIE, 10702, 1070250
Sullivan, P. W., Winn, J. N., Berta-Thompson, Z. K., et al. 2015, ApJ, 809, 77
Wright, E. L., Eisenhardt, P. R. M., Mainzer, A. K., et al. 2010, AJ, 140, 1868
Yee, S. W., Petigura, E. A., & von Braun, K. 2017, ApJ, 836, 77
Yu, X., He, C., Zhang, X., et al. 2021, NatAs, 5, 822
Zechmeister, M., Reiners, A., Amado, P. J., et al. 2018, A&A, 609, A12
Ziegler, C., Law, N. M., Baranec, C., et al. 2018, AJ, 156, 259